



Imaging with diffractive axicons rapidly milled on sapphire by femtosecond laser ablation

Daniel Smith¹ · Soon Hock Ng¹ · Molong Han¹ · Tomas Katkus¹ · Vijayakumar Anand¹  · Karl Glazebrook² · Saulius Juodkazis^{1,3}

Received: 3 July 2021 / Accepted: 11 October 2021 / Published online: 22 October 2021
© The Author(s), under exclusive licence to Springer-Verlag GmbH Germany, part of Springer Nature 2021

Abstract

Fabrication of large area (sub-1 cm cross-section) micro-optical components in a short period of time (~ 10 min) and with lesser number of processing steps is highly desirable and cost-effective. In the recent years, femtosecond laser fabrication technology has revolutionized the field of manufacturing by offering the above capabilities. In this study, a fundamental diffractive optical element, binary axicon–axicon with two phase or amplitude levels, has been designed in three configurations namely conventional axicon, photon sieve axicon (PSA) and sparse PSA and directly milled onto a sapphire substrate. The fabrication results revealed that a single pulse burst fabrication can produce a flatter and smoother profile than pulse overlapped fabrication which gives rise to surface damage and increased roughness. The fabricated elements were processed in IsoPropyl alcohol and potassium hydroxide to remove debris and redeposited amorphous sapphire. An incoherent illumination was used for optical testing of the components and a non-linear optical filter was used for cleaning the noisy images generated by the diffractive optical elements.

Abbreviations

PSA	Photon sieve axicon
DOE	Diffractive optical elements
FWHM	Full width at half maximum
NLR	Non-linear reconstruction
IPA	Isopropyl alcohol
LED	Light emitting diode
DOF	Depth of focus
M	Molar
KOH	Potassium hydroxide

SEM	Scanning electron microscope
UV	Ultraviolet
IR	Infrared
FBMS	Fixed beam movable stage
NIR	Near infrared
NA	Numerical aperture
PSO	Position sensitive output

1 Introduction

Generation and precise control of optical fields is crucial in many optical instruments and imaging systems [1]. The optical fields can be engineered using optical components belonging to different categories such as refractive [2], diffractive [2], reflective [3], metaoptics [4–6], polarization optical components such as Q-plates [7], and liquid crystal optical components [8] based on the principle of operation. Depending upon the degree of control needed on the components of the optical field such as amplitude, phase and polarization, the complexity involved in design as well as fabrication varies. Next to the fully matured refractive optical technology, diffractive optics remains as the most widely used mode of beam control offering easier design, reasonable fabrication costs, and reaching diffraction efficiency closer to the values of refractive elements. Diffractive

Daniel Smith, Soon Hock Ng and Molong Han contributed equally to this work.

✉ Vijayakumar Anand
vanand@swin.edu.au

¹ School of Science, Optical Sciences Centre and ARC Training Centre in Surface Engineering for Advanced Materials (SEAM), Swinburne University of Technology, Hawthorn, VIC 3122, Australia

² School of Science, Centre for Astrophysics and Supercomputing, Swinburne University of Technology, Hawthorn, VIC 3122, Australia

³ School of Materials and Chemical Technology, Tokyo Tech World Research Hub Initiative (WRHI), Tokyo Institute of Technology, 2-12-1, Ookayama, Meguro-ku, Tokyo 152-8550, Japan

optics plays an important role in many areas of research such as optical trapping and tomography [9], computer generated holography [10], biomedical applications [11], integrated optics [12], display technology and serve also as components in augmented and mixed reality glasses [8].

The diffractive optical elements (DOEs) can be manufactured using different techniques such as photolithography [13], electron beam lithography [14], ion beam lithography [15], depending upon the feature sizes and area of the design. All of the above methods are not only time-consuming, but also have higher operating costs resulting in an increase in the cost of the DOEs. Except ion beam lithography, the other two methods cannot fabricate elements directly on to the substrate and therefore, require additional processing steps such as reactive ion etching to transfer the pattern from the resist layer to the substrate which increases the cost of manufacturing further. The electron beam and ion beam lithography methods are not suitable for fabrication of large area DOEs. Even though it may be argued that photolithography can transfer large area patterns, the time is still spent on fabrication of the mask. Therefore, except for mass production, even photolithography cannot be considered as a rapid fabrication system.

In the recent years, there has been a revolution in manufacturing of DOEs due to the advent of femtosecond ablation techniques [16–19]. They not only offer capabilities to manufacture large area DOEs, but also can reach subwavelength features by the generation of harmonics. Furthermore, the vacuum conditions and other environmental isolation needed for electron and ion beam optics can be avoided in the femtosecond fabrication system. All of the above makes femtosecond fabrication systems superior to the existing methods on various technological and economical fronts. One current limitation of fs-laser fabrication is in its low capability to deliver practical solution for large area (mm-to-cm) scale micro-optical elements. This limitation is especially felt for large scale optical systems encountered in astronomy where meter-scale lenses and mirrors are used. For any optical system, the best light energy collection and transfer has to be achieved, which is handled via the best possible channeling of the etendue throughout the optical system from collection to detection (or imaging). The etendue $E = S \times Q$ defined by the area S of the beam and the solid angle Q under which beam passes the surface. Optical elements with large surface area are required for best collection of light in low intensity light collection setups. Here we explore large area and fast laser fabrication which can become practical for astro-photonics.

In the recent years, there has been a shift in focus in imaging research from using coherent light sources to incoherent ones due to the many advantages such as broad applicability, low cost, and high resolving power [20]. A significant proportion of incoherent imagers are based on coded aperture

imaging (CAI) method in which the light diffracted from an object was scattered and by computationally processing of the scattered intensity distributions with point spread functions (PSFs) the object information was reconstructed in multiple dimensions—3D space and spectrum. The need for scattering makes CAI methods not suitable for power sensitive application areas such as fluorescence microscopy and astronomical imaging. Furthermore, the design and fabrication of a reasonably efficient coded aperture is complicated. In view of the above facts, in this study, a binary axicon is considered. Binary axicon has one of the simplest structures consisting of concentric rings with same period enabling easy design and fabrication. Binary axicon has a relatively higher signal to noise ratio than coded apertures and has a high focal depth capable of generating sharp object information from multiple planes on the sensor. An axicon has a low axial resolution and so it is difficult to discriminate information from nearby planes as in CAI method. However, for cases like astronomical imaging, the object information is sparsely distributed and so an axicon may be suitable than a lens or a CAI method.

In this study, the femtosecond fabrication by ablation has been implemented to rapidly fabricate two-level axicons directly on to sapphire substrates. The axicons were realized in conventional ring as well as sieve configurations. The focus of this study is on the rapid fabrication approach for manufacturing large area diffractive optical elements for astronomical imaging applications. This manuscript consists of four sections. The calculation of diffracted intensity distribution and the simulation results are presented in the next section. The third section contains the fabrication procedure and characterization and optical experiments and beam cleaning procedure. The summary and conclusion are presented in the final section.

2 Methodology

In most of the earlier studies on beam characteristics of axicon only a coherent illumination is considered [21–23]. In this study, the beam characteristics are investigated for a spatially incoherent illumination as it is easily available at a low cost and will be highly relevant to large scale and astronomical applications where large area devices are often required which in turn can be manufactured using femtosecond fabrication systems. For a single point object, the behaviour of a coherent light is like that of an incoherent one [20]. However, when there is more than one point, then the optical system differs hugely between coherent and incoherent illuminations. The optical configuration is shown in Fig. 1 in which the light diffracted from a point object is incident on a diffractive axicon and the intensity distribution

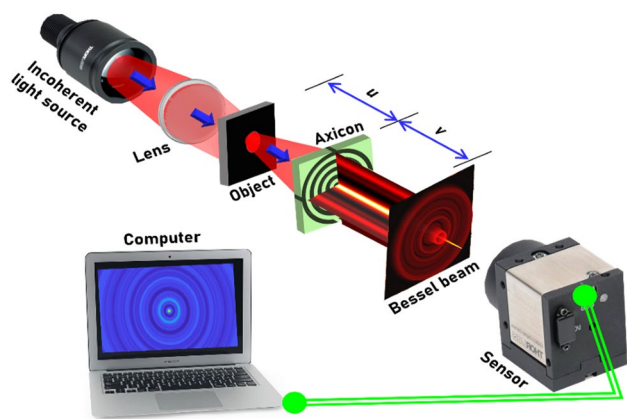


Fig. 1 Optical configuration for the generation of Bessel beams by a diffractive axicon

is recorded. The distance between the object and the axicon is u and the distance between the axicon and the sensor is v .

The binary axicon can be realized either as concentric rings or rings filled with discs similar to a photon sieve [24]. While the former with concentric rings has been widely used, only a few reports are available on axicons with sieve configuration. The rationale for comparing a conventional axicon with a photon sieve axicon (PSA) is that the fabrication using femtosecond ablation occurs point by point and it is much easier to realize an axicon as a PSA (disconnected discs) rather than in conventional type (overlapped discs). The radii of zones of a binary axicon can be given as,

$$r_{1-n} = n\Lambda, \tag{1}$$

where Λ is the period of the axicon and n is an integer. The phase of a binary axicon can be expressed as,

$$\Phi_{\text{Axicon}} = \begin{cases} \pi, & r_{1-n+1/2} \leq R \leq r_{1-n+1} \\ 0, & \text{elsewhere} \end{cases} \quad \text{where } R = \sqrt{x^2 + y^2}. \tag{2}$$

The phase of a PSA is mathematically complicated as it is made up of circular discs of the same diameter instead of rings of varying diameters as in an axicon. A two-step process is proposed to design the PSA with polar coordinates (R, φ) where $\varphi = \tan^{-1}(y/x)$. In the first step, a mask consisting of Delta functions located at the x and y coordinates of the centers of the discs of diameter $\Lambda/2$ is generated. The centers of the circular discs can be located only at specific radial values given as,

$$r_{2-n} = (4n - 1)\Lambda/4. \tag{3}$$

The circular discs cannot be tightly arranged in the ring of an axicon as the circumference given as $2\pi r_{2-n}$ cannot be an integral multiple of Λ for all values of r_{2-n} . The difference between the above two values is given as,

$$L(r_{2-n}) = 2\pi r_{2-n} - \{\text{floor}(4\pi r_{2-n}/\Lambda)\}\Lambda/2, \tag{4}$$

where *floor* function converts an input real number x into the greatest integer less than or equal to x . The increment in location needed for every disc is,

$$\Delta(r_{2-n}) = L(r_{2-n})/\{\text{floor}(4\pi r_{2-n}/\Lambda)\}. \tag{5}$$

The values of the angles are given as,

$$\theta_m(r_{2-n}) = [m\{\Lambda + \Delta(r_{2-n})\}]/r_{2-n}, \tag{6}$$

where m varies from 0 to $\text{floor}(4\pi r_{2-n}/\Lambda)$. The mask consisting of Delta functions is given as,

$$\text{Mask} = \begin{cases} \delta, & R = r_{2-n} \text{ and } \varphi = \theta_m \\ 0, & \text{elsewhere.} \end{cases} \tag{7}$$

At the end of the first step, the map of Delta functions is obtained for mounting the circular discs in the next step. To generate the mask of PSA (M_{PSA}), it is just sufficient to carry out a 2D convolution of the Mask function with a Circ function which is a circular top hat with a radius given by,

$$M_{\text{PSA}} = \text{Mask} \otimes \text{Circ}(\Lambda/2), \tag{8}$$

where ‘ \otimes ’ is a 2D convolutional operator. The phase of the PSA is given as, $\Phi_{\text{PSA}} = \exp(j\pi M_{\text{PSA}})$.

Let us consider a point object located at a distance of u from the diffractive axicon emitting light with an amplitude of $\sqrt{I_o}$. The complex amplitude reaching the axicon is given as,

$$\psi_1 = C_1 \sqrt{I_o} Q(1/u) L(\bar{r}_o/u), \tag{9}$$

where,

$$Q(1/u) = \exp[j\pi R^2/(\lambda u)], \tag{10}$$

$$L(\bar{o}/u) = \exp[j2\pi(o_x x + o_y y)/(\lambda u)], \tag{11}$$

and C_1 is a complex constant and there is no linear phase associated with a point object in this case as the optical axis is assumed to match with the centres of all the optical elements. The complex amplitude after the binary axicon and PSA is given as,

$$\psi_2 = C_1 \sqrt{I_o} L(\bar{r}_o/u) Q(1/u) \exp(-j\Phi_{\text{DOE}}), \tag{12}$$

where $\Phi_{\text{DOE}} = \Phi_{\text{Axicon}}$ when an axicon with concentric rings is used and $\Phi_{\text{DOE}} = \Phi_{\text{PSA}}$ when an axicon with sieve configuration is used. The intensity pattern observed at a distance of v from the DOE is given as a convolution of the complex amplitude with the quadratic phase function $Q(1/v)$,

$$I_v(\bar{r}_s, \bar{r}_o, u) = \left| C_1 \sqrt{I_o} L\left(\frac{\bar{r}_o}{u}\right) Q\left(\frac{1}{u}\right) \exp(-j\Phi_{\text{DOE}}) \otimes Q\left(\frac{1}{v}\right) \right|^2. \quad (13)$$

From Eq. (13), if the Φ_{DOE} equals $(\pi R^2/\lambda)(1/u + 1/v)$, then in the observation plane a focused point is obtained as the other phase components are cancelled. But for an axicon, the behaviour is quite interesting as it has constant radial spatial frequency. Within the focal depth of the axicon, there is always a radial region of the axicon which has a phase distribution same as $(\pi R^2/\lambda)(1/u + 1/v)$. This region is responsible for generating the central maximum of the Bessel function and the other radial regions which does not match the above phase distribution generate ring patterns around the central maximum. Higher the phase difference,

the larger the diameter of the ring and the smaller is the energy density [25]. The intensity for a 2D object O can be expressed as $I_o = O \otimes I_v$. Unlike a coherent source, where the complex amplitude is convolved, here only the intensity distribution is convolved as there is no spatial coherence present to generate the interference terms.

The images of the simulated axicon and PSA with same period are shown in Fig. 2a, b, respectively. The images of the diffraction pattern at the same distance for axicon and PSA are shown in Fig. 2c, d, respectively and their normalised intensity profiles are shown in Fig. 2e, f, respectively. There are interesting observations when comparing the diffraction patterns of axicon and PSA. The central maximum is sharper for axicon than PSA and the sidelobes of axicon appear less strong than that of the PSA. The two intensity

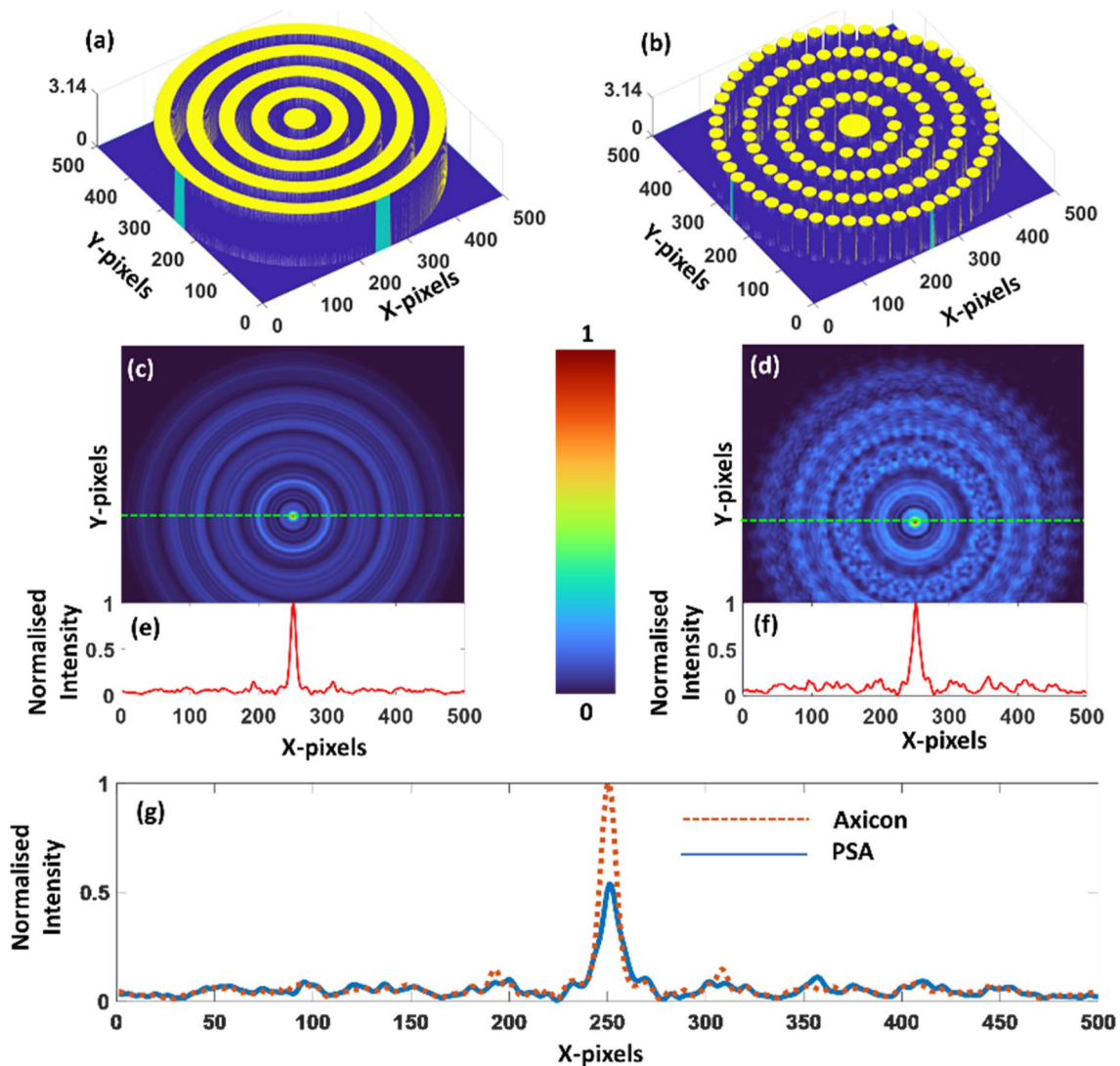


Fig. 2 Phase profile of **a** axicon and **b** PSA for a simulation wavelength $\lambda=617$ nm. Intensity distribution obtained for **c** axicon and **d** PSA. Locally normalised intensity profile of the line data ($y=0$) for

e axicon and **f** PSA. **g** Universally normalised intensity profile of the line data ($y=0$) for axicon and PSA

distributions were normalised over the maximum of both and the intensity profile is compared as shown in Fig. 2g. It is seen that axicon has a higher contrast of central maximum to the surrounding rings compared to that of PSA and the full width at half maximum (FWHM) obtained for axicon is smaller than that of PSA. This behaviour is different from the observations made with a Photon sieve Fresnel lens [26], where an improvement in the resolution was observed. The difference may be accounted to the difference between the areas of the two-phase levels. In the previous simulation studies, the areas were made equal to obtain the maximum efficiency in addition to maintaining the phase difference between two levels at π for a two-level structure [2]. Due to the replacement of rings by circular discs, this condition cannot be met accurately. A previous study on PSA directly fabricated on the tip of optical fibre exhibited characteristics of an axicon [27]. To further evaluate the focal characteristics, the axial characteristics are studied for axicon and PSA under ideal conditions. The axial variation of the intensity distributions at ($y=0$) line for axicon and PSA are shown in Fig. 3a, b, respectively. Comparing the above two figures, it is seen that the performances are similar. From the simulation studies, it is seen that approximating a binary axicon using circular discs does not yield a better performance but reduces the contrast of the central maxima with respect to the surrounding ring patterns. However, the fabrication of PSA

using femtosecond ablation is relatively easier than the fabrication of a conventional axicon.

The next step is to study the imaging performances of axicon and PSA using a test object. All experiments for this study have been carried out at Nanolab, Swinburne University and so the test object has been selected as the letters of “Nanolab” in arial font as shown in Fig. 4a. The image of the object obtained using a Fresnel lens, axicon and PSA are shown in Fig. 4b–d, respectively. It is seen that the sidelobes generated by axicon affects the imaging quality drastically as expected and the results of PSA are distorted more than a conventional axicon. Since the imaging system using PSA is a linear shift-invariant system, it is possible to obtain an image without the background noise using cross-correlation with the point spread function (PSF). Cross-correlation is one of the most widely used reconstruction methods in coded aperture imaging systems such as coded aperture correlation holography (COACH) [28] and interferenceless-COACH (I-COACH) [29]. Recently, it was found that non-linear reconstruction method was the optimal correlation-based reconstruction method for scattering-based linear shift-invariant system [30]. Can the NLR be applied to this method of imaging using PSA?

In I-COACH, every point in the object space is mapped to a random intensity distribution in the sensor plane. When there are many points in the same plane, every point generates the same random intensity distribution but shifted

Fig. 3 Locally normalised axial intensity distribution along the line ($y=0$) for **a** axicon and **b** PSA

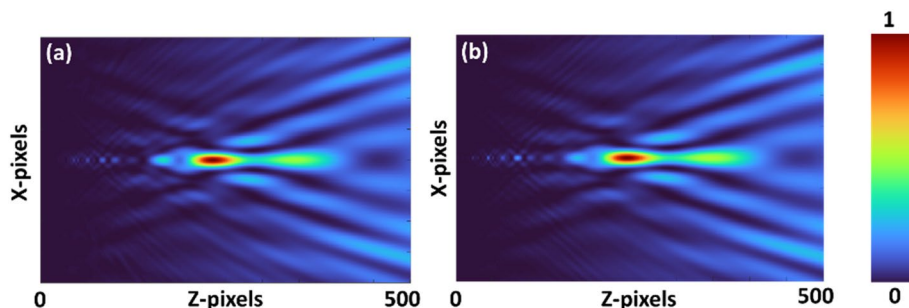
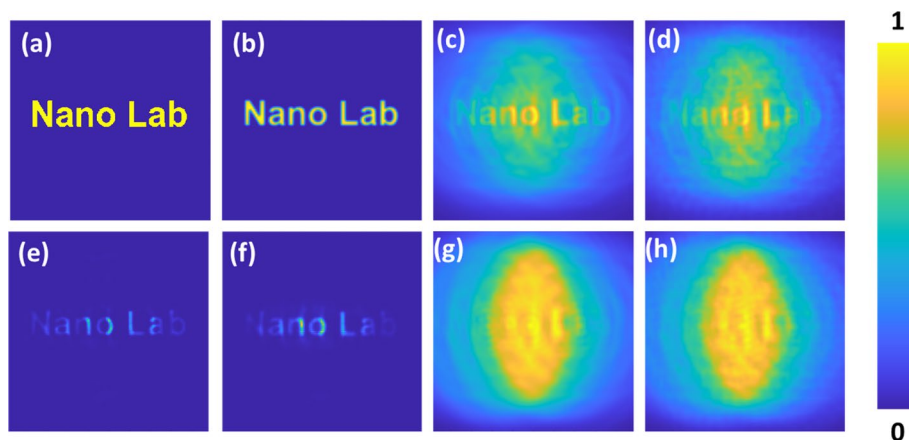


Fig. 4 Image of the **a** test object. Image of the object generated by a **b** Fresnel lens, **c** axicon and **d** PSA. Computationally cleaned image by applying NLR for **e** axicon and **f** PSA. The images obtained for coherent illumination for **g** axicon and **h** NLR



depending upon the linear phase they possess. In an incoherent imaging system, these random intensity distributions are summed. This is the meaning of linear shift invariant system in intensity. In I-COACH, when the point object is axially shifted, the random intensity distribution changes. In the current system, every point in the object space is mapped to a Bessel-like intensity distribution. When there are many points, shifted Bessel-like intensity distributions are generated depending upon the linear phase and all such Bessel-like intensity distributions are summed in the sensor plane. However, unlike I-COACH, when the axial location is changed, the intensity distribution does not vary within the focal depth. In both I-COACH and the imaging with PSA, the object information can be reconstructed by a cross-correlation between the multi-points intensity distribution and the PSF. In I-COACH, to reconstruct the object at a different plane, the PSF at that plane is needed. In imaging with PSA, different planes of the object can be reconstructed using the same PSF. Non-linear reconstruction is the optimal correlation obtained by tuning the magnitudes of spectrum of the object intensity and PSF until a minimum entropy is obtained. This approach can be applied to any linear shift-invariant system. NLR is a pattern recognition operation with a physical meaning of scanning the PSF over the object intensity pattern and finding the value of similarity at every location. So, while applying NLR, a Bessel-like intensity pattern obtained for a single point (by PSA) is once again converted into a point. Consequently, an image with background is converted to an image without background during this operation yielding a cleaner image. This is the rationale for applying NLR to this method [30–32].

The cleaned image by NLR is given as,
$$I_R = \left| \mathcal{F}^{-1} \left\{ |\tilde{I}_v|^\alpha \exp [i \arg (\tilde{I}_v)] |\tilde{I}_o|^\beta \exp [-i \arg (\tilde{I}_o)] \right\} \right|$$
, where α and β are tuned to obtain the lowest entropy and \arg refers to the phase. The images generated by axicon and PSA after applying NLR is shown in Fig. 4e, f, respectively. To show the difference between the use of coherent and incoherent illumination, the results obtained for coherent light source for an axicon and PSA are shown in Fig. 4g, h, respectively. Comparing the results obtained for spatially incoherent light with those of coherent light, the quality of images was found to be better for spatially incoherent illumination than coherent due to the lack of mutual interference.

Another important observation is that the intensity distribution of axicon and PSA are similar in the central region while they are quite different at the outer regions (refer Fig. 2). The random change in the location of the discs and the spacing between the discs at every consecutive zone disturbs the diffraction pattern resulting in the interesting intensity distribution for PSA. To understand the axial characteristics of axicon and PSA, the intensity distribution I_v

was simulated for different distances of v from $v - \Delta$ to $v + \Delta$ and cross-correlated with the intensity distribution at v as $I_v * I_{v \pm \Delta}$, where ‘*’ is a 2D correlation operator. The intensity distributions for some distances and the plot of the axial correlation values are shown for both axicon and PSA in Fig. 5. The case for a diffractive lens is shown for reference. From this study, it seems that a PSA has a higher axial resolution than an axicon. The randomness associated with the distribution of disc suppresses the peaks around the central maximum. From an imaging point of view, the PSA has a slightly better performance than an axicon. When imaging a thick object and focusing a plane of that object, the information from other planes will be of slightly lower intensity in the case of PSA when compared to an axicon. Compared to a lens, both PSA and axicon have a significantly lower axial resolution. However, the intended area of application, i.e., 3D imaging of sparse objects, the high focal depth of PSA and axicon will be useful.

3 Experiments

3.1 Fabrication

The fabrication was carried out on sapphire substrate with a thickness of 500 μm and index of refraction $n_s = 1.76$. To have π phase difference between the two levels the thickness needed to be milled is given as $t = \lambda/2(n_s - 1)$ which is $\sim 0.41 \mu\text{m}$ for $\lambda = 617 \text{ nm}$ which is the wavelength of the source used for optical testing. The substrate was cleaned prior to fabrication with acetone and iso-propyl alcohol

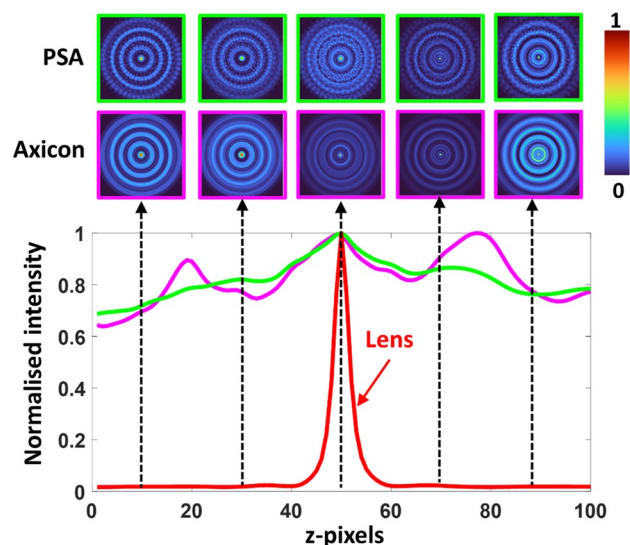


Fig. 5 Plot of $I_v * I_{v \pm \Delta}$ for different distances for axicon (pink), PSA (green) and a lens (red). The intensity distributions for axicon, and PSA for some distances have been provided

(IPA) and blown dry. Three optical devices, namely an axicon, a PSA and a sparse PSA were fabricated. The fabrication was carried out using a Pharos laser (Light Conversion, Lithuania) operating at 200 kHz repetition rate, $\lambda = 1030$ nm wavelength, 2.5 W average power, 230 fs pulse duration and $5\times$ magnification, $NA = 0.14$ numerical aperture Mitutoyo Plan Apo NIR infinity corrected objective. Two pulse bursts per ablation spot was used (with an exception for the axicon that did not use a pulse burst) in combination with pulse energy after the objective attenuated to $5\ \mu\text{J}$ to achieve the design ablation depth and the ablated spot diameter of $d = 8.9\ \mu\text{m}$. The diameter of ablated spot was closely matching the diameter for the used NA: $d = 2w = 1.22\ \lambda/NA$, where w is the waist of the beam at focus. The peak intensity of a $5\ \mu\text{J}$ pulse (peak intensity is twice the average) is $69\ \text{TW}/\text{cm}^2$ at the fluence of $16\ \text{J}/\text{cm}^2$. This is markedly larger than the ablation threshold of sapphire at $\sim 2\ \text{J}/\text{cm}^2$ and $\sim 10\ \text{TW}/\text{cm}^2$. The speed of Aerotech positioning stages was set to $2\ \text{mm}/\text{s}$. Stage travel with position sensitive output (PSO)

mode was used to ensure accurate pulse spacing. The fabrication code was written in SCA software (Workshop of Photonics Altechna, Lithuania). The code comprised of concentric circle commands with circle radius increasing by $16\ \mu\text{m}$ till the overall design diameter reached $5\ \text{mm}$. Laser pulse spacing in a given circle was set to be $5\ \mu\text{m}$, $8\ \mu\text{m}$, and $12\ \mu\text{m}$ for respectively the axicon, the PSA, and the sparse PSA fabrications. The Pharos system unlike electron beam lithography system always works in fixed beam movable stage mode (FBMS) mode which is a special case in lithography systems such as RAITH150². Conventional raster and serpentine scanning approaches are time consuming as every pixel of the design must be scanned. In this study, time efficient circular scanning procedure was selected where the pixel locations were selected for the beam to traverse and the stage was moved only to those locations as shown in Fig. 6a. The scanning procedure started from the centre and moved gradually outward following the coordinate map. In this way, the fabrication time was reduced by at least half of

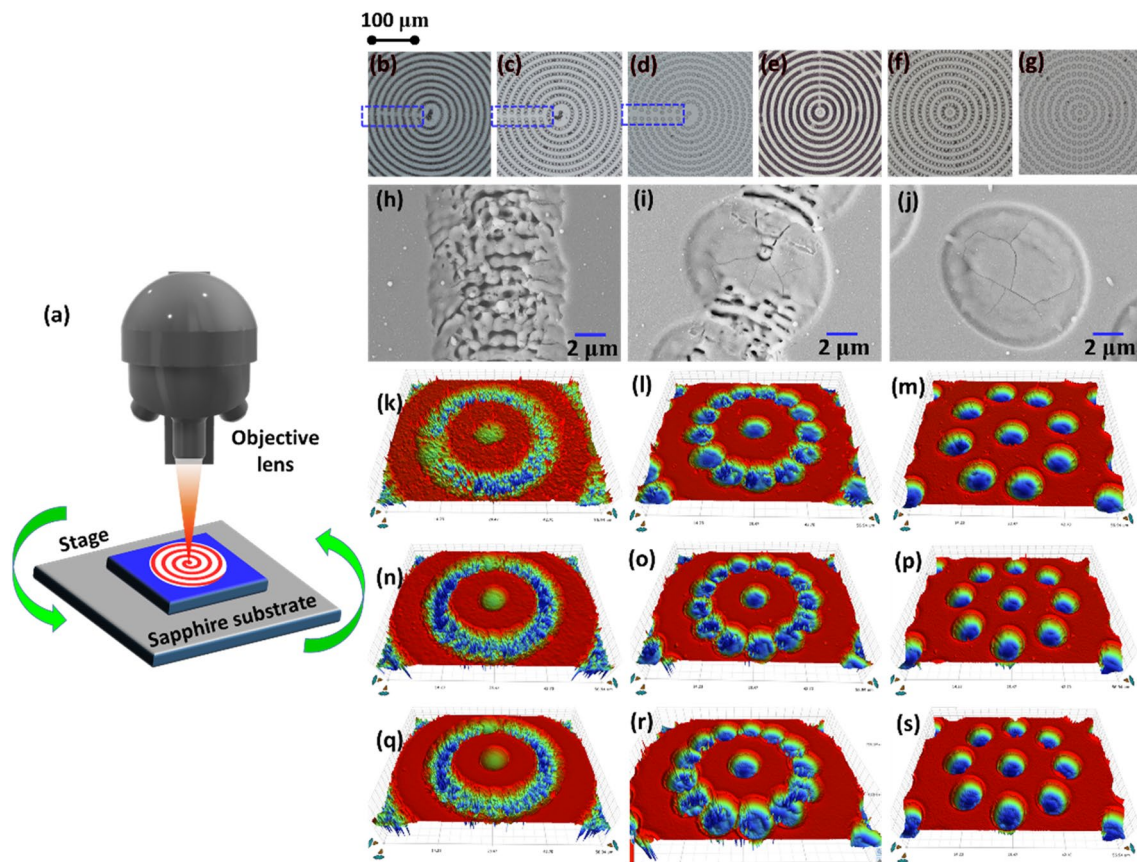


Fig. 6 **a** Schematic of the scanning procedure. Optical microscope images of the central part of **b** axicon, **c** PSA and **d** sparse PSA with stitching and stigmatism errors. Optical microscope images of the central part of **e** axicon, **f** PSA and **g** sparse PSA after the correction of stitching and stigmatism errors. SEM images of a single pulse fabrication for **h** axicon, **i** PSA and **j** sparse PSA; ripples with

period $\sim 1\ \text{mm} \approx 1$ are recognizable in the strongly overlapped pulse exposure regions. Surface profiles of **k** axicon, **l** PSA and **m** sparse PSA, after femtosecond fabrication. Surface profiles of **n** axicon, **o** PSA and **p** sparse PSA after ultrasonic cleaning in IPA and surface profiles of **q** axicon, **r** PSA and **s** sparse PSA after KOH etching

that of conventional scanning approaches. The fabrication time for the sparse PSA, PSA and axicon was approximately 10 min. When the stage moved to the coordinates, a laser pulse (single pass) ablates the corresponding voxels (volume element, i.e., a 3D pixel).

In the first step, the effect of stitching error arising due to the condition that the circumference of the zones is not equal to the integral multiples of $\lambda/2$. The optical microscope images of the fabricated axicon, PSA and sparse PSA are shown in Fig. 6b–d, respectively. The stitching error is clearly visible. In addition to the stitching error, there was error due to stigmatism in the stage resulting in oval-shaped zones. The error compensation terms were introduced in the code to reduce both the stitching error and stigmatism. The optical microscope images after correction are shown in Fig. 6e–g, respectively. The SEM images of a single disc for axicon, PSA and sparse PSA are shown in Fig. 6h–j. It can be seen that with the overlap of pulses in PSA and axicon, the surface is damaged more and becomes rough due to ripple formation [33] while the sparse PSA without disc overlap has a smoother and nearly flat surface with only cracks visible at the molten region on the bottom. A fast thermal quenching of shallow melt pool is the most probable cause of formation of nano-cracks; note the melting temperature of sapphire is 2040 °C. A remarkable feature of the used two-pulse ablation was a flat bottom of the ablation pit. The apparent melting was contributing to the flatness of ablation site; however, the other contribution should be in the profile of energy deposition. The die-met transition, when dielectric is transferred to the metallic plasma state with permittivity decreasing to $e = n^2 = 0$ at the dielectric breakdown [34], is defining the lateral absorption profile. For a Gaussian-like intensity at the focus, the most intense central region is turning into the most reflective during the laser pulse, hence, less energy is deposited to the sample. This qualitatively explains the ablation profile which would be expected for a hat-top intensity profile (rather than the Gaussian). The detailed mechanism of ablation is out of scope of this study focused on optical performance, however, is worth of a deeper investigation.

The rough surfaces of PSA and axicon are expected to scatter light more resulting in lower efficiency in the first diffraction order. After fabrication, it was noted that there was redeposition of debris both on the milled and unmilled areas of the device. Two step cleaning procedures were carried out. After femtosecond fabrication, the sample was cleaned in IPA in the ultrasonic bath for 5 min. The surface profiles of the axicon, PSA and sparse PSA before and after cleaning are shown in Fig. 6k–p, respectively. After the first cleaning, most of the debris are removed. The next cleaning was carried out with a KOH solution with (2 M concentration for 2 h) to remove the redeposited amorphous sapphire and there was further improvement rendering an even smoother

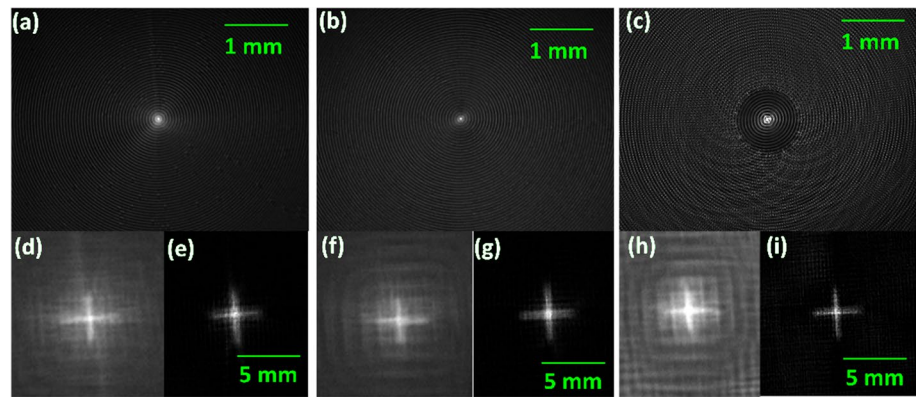
profile [35] for axicon, PSA and sparse PSA as shown in Fig. 6q–s. The average depth values measured for the axicon, PSA and sparse PSA were 360 nm, 416 nm, 420 nm, respectively. This required depth for a p-phase shift was achieved in a two-pulse irradiation without change of the focal position. The Rayleigh length (half of depth-of-focus DOF) is $z_R = pw^2/l = 61.4$ mm. This large DOF increase tolerance of high-fidelity fabrication over large areas when some tilt of a surface plane can be expected. The dark regions in the microscope images and the higher roughness in surface profiles indicates that there was some amount of redeposition of the material into the ablated area due to the overlap of the voxels during fabrication. This redeposition is dependent upon various factors such as the pulse energy, material characteristics such as melting point, crystalline or amorphous.

3.2 Optical testing

The optical testing was carried out using a high-power LED from Thorlabs [M617L3, $\lambda_c = 617$ nm, full width at half maximum (FWHM) = 18 nm] and a spectral filter was used at 600 nm with a width of 10 nm to improve the temporal coherence. A pinhole with a size of 100 μm and a cross-shaped object were used for imaging. A $3\times$ magnifying system was used to reimage the intensity distribution that is close to the DOEs on an image sensor (Thorlabs DCU223M, 1024 pixels \times 768 pixels, pixel size = 4.65 μm). The DOEs were mounted one after the other and the intensity distributions were recorded. The intensity distributions recorded at a distance of 5 mm for the axicon, PSA and sparse PSA are shown in Fig. 7a–c, respectively. A cross object was then mounted instead of the pinhole and the intensity patterns were recorded at 3 cm from the DOEs. The images of the cross object recorded for the axicon, PSA and sparse PSA are shown in Fig. 7d, f, h, respectively. The images were cleaned using the images obtained for a pinhole and the NLR method and the cleaned images are shown in Fig. 7e, g, i, respectively. To improve the cleaning results, additional filters such as median filter and correlation filters were used as demonstrated in [36]. The images after cleaning for axicon, PSA and sparse PSA appear similar.

Therefore, it is feasible to use a sparse axicon instead of a regular axicon for imaging applications. By virtue of a wide spectral transparency of sapphire from UV to IR, optical elements with ~ 1 cm cross section can be made within ~ 10 min which allows for a wider use of such prototyping for more complex optical systems. It must be noted that the cleaning procedure does not require the recording of the PSF exactly at the same location as the object owing to the high focal depth of the imager. For the same reason, while cleaning images of thick objects the planes that are out of focus will have a higher intensity as the plane in focus. Consequently, if the information of

Fig. 7 Intensity distributions recorded for a pinhole at distances 5 mm for **a** axicon, **b** PSA and **c** sparse PSA. Recorded intensity distributions for a cross-shaped transmission object at 5 mm for **d** axicon, **f** PSA and **h** sparse PSA. Cleaned images of cross for **e** axicon, **(g)** PSA and **i** sparse PSA



two planes overlap laterally then the information could not be perceived accurately. The PSF recorded at a single plane can be used to clean the image information corresponding to many planes due to the high focal depth of PSA and axicon. The image cleaning results for the intensity distributions recorded for the cross object at 5 cm (Fig. 8a) and 6 cm (Fig. 8b) using pinhole intensity distributions recorded at 5 mm are shown for axicon and PSA as shown in Fig. 8c, d, respectively. Since the cross object is a simple object, the cleaning may not appear significant. A synthetic object consisting of the letters 'APHB' was used next and the corresponding intensity distributions for PSA were synthesized by convolving the intensity distributions recorded for a pinhole with the object function. The intensity distribution of the synthetic object at two planes 5 cm and 6 cm are shown in Fig. 8e, f, respectively. The cleaned images using the pinhole recording at 5 mm are shown in Fig. 8g, h, respectively.

4 Conclusion

Rapid fabrication of large area DOEs using the femtosecond laser fabrication system has been investigated. A simpler design with the function of a binary axicon was used for the study. The fabrication time was only 10 min using the femtosecond fabrication method for a large area of 5 mm × 5 mm. The binary axicon was realized in three configurations namely conventional axicon, PSA and sparse PSA. It was noticed that when the beam overlaps during milling results in redeposition of material resulting in a lower depth than the case without beam overlap which goes against the common belief that overall higher exposure with beam overlap increases the depth. In addition, the case with beam overlap has a higher roughness value than the case without beam overlap. This increase in roughness is partly contributed by the redeposition and partly due to light-matter interaction at temperature changes caused by ablation by the previous pulse. Reduction of debris and mechanism of ripple-free deep ablation

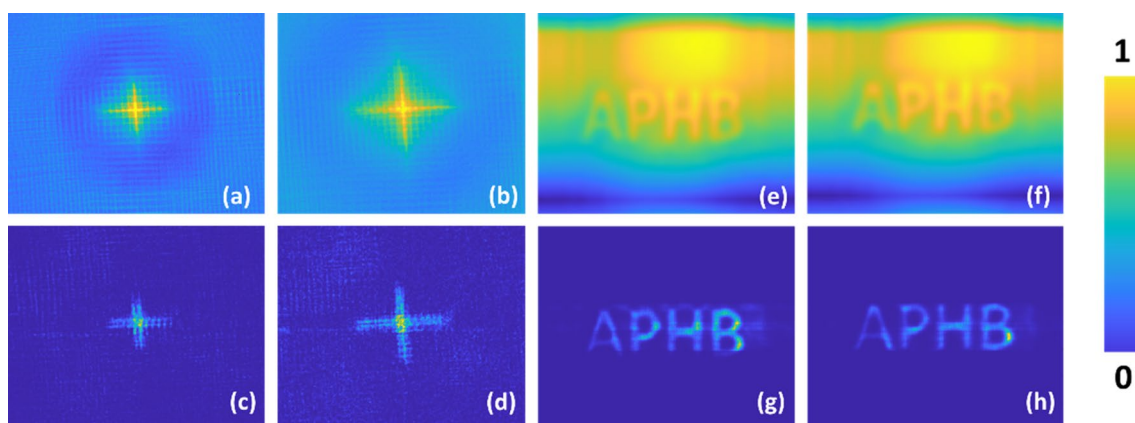


Fig. 8 Intensity distribution of cross object recorded at **a** $z=5$ cm and **c** $z=6$ cm and the corresponding cleaned images **c** $z=5$ cm and **d** $z=6$ cm, respectively. Intensity distribution of synthetic object

'APHB' recorded at **e** $z=5$ cm and **f** $z=6$ cm and the corresponding cleaned images **g** $z=5$ cm and **h** $z=6$ cm, respectively

at high irradiance which exceeds ablation threshold more than an order of magnitude are directions for future investigations which were not practical at low repetition rates [37].

One interesting outcome of this study is that it seems it may be necessary to approximate the design of the DOE functions as in this case where a sieve configuration was used instead of rings to achieve a milling favorable design. As is seen in this study, the intensity distributions obtained for the sieve configuration is similar to that of the conventional axicon with a slight loss of lateral resolution and increase in axial resolution. Therefore, it should be possible to modify the design of DOEs without compromising the diffraction performances and at the same time achieve high fabrication accuracy without material redeposition and increase in surface roughness.

Some of the recent studies on controlling the distribution of debris using externally applied electric and magnetic fields offer opportunities to control the light-matter interactions and achieve better fabrication results [38, 39]. We believe that the direction of research will enable the fabrication of large area structures suitable for incoherent illumination and astronomical imaging applications. With the introduction of spatial multiplexing [40], optimization [41] and redesigning of DOEs, the performance of the femtosecond fabrication system can be improved further. Astronomical imaging is one of the areas which require large area optical devices with capabilities to perform a high signal to noise ratio. We believe that the femtosecond ablation-based rapid fabrication and computational optics in tandem will lead to the development of advanced astronomical imaging technologies. Some of the latest developments in astronomical spectral imaging technologies such as FOBOS [42] require numerous micro-optical devices for the successful implementation of free space to fiber bundle coupling for spectral imaging. We believe that the current work consisting of rapid fabrication and beam cleaning will support retrieving spatial information in addition to the recorded spectral information [43].

Acknowledgements We are grateful to the Workshop of Photonics, Ltd. for femtosecond laser fabrication system acquired via technology transfer project. We acknowledge funding for the Nanolab by Swinburne University of Technology (SUT). DS is grateful for support via Honors and MH via PhD programs at SUT.

Author contributions Light matter interaction and dynamics conceptualization—SJ; fabrication—DS, SHN, MH and TK; characterization—MH, DS, SHN, VA and TK KOH etching—SHN, VA and DS; simulation—VA and DS; optical testing—VA, SHN and DS; manuscript writing—VA and SJ; review, editing and proof reading—all the authors; project guidance—KG, SJ; resources—SJ; funding—SJ.

Funding ARC LP190100505 is acknowledged for funding.

Data availability The datasets used and/or analysed during the current study are available from the corresponding author on reasonable request.

Declarations

Conflict of interest The authors declare no conflicts of interest.

References

1. F.M. Dickey, S.C. Holswade, D.L. Shealy (eds.), *Laser Beam Shaping Applications* (CRC Press, Boca Raton, 2005)
2. A. Vijayakumar, S. Bhattacharya, Design and fabrication of diffractive optical elements with MATLAB (2017)
3. J. Liang, R.N. Kohn Jr., M.F. Becker, D.J. Heinzen, High-precision laser beam shaping using a binary-amplitude spatial light modulator. *Appl. Opt.* **49**(8), 1323–1330 (2010). <https://doi.org/10.1364/ao.49.001323>
4. L. Wang, S. Kruk, H. Tang, T. Li, I. Kravchenko, D.N. Neshev, Y.S. Kivshar, Grayscale transparent metasurface holograms. *Optica* **3**(12), 1504–1505 (2016). <https://doi.org/10.1364/optica.3.001504>
5. A. Epstein, G.V. Eleftheriades, Huygens' metasurfaces via the equivalence principle: design and applications. *J. Opt. Soc. Am. B* **33**(2), A31–A50 (2016). <https://doi.org/10.1364/josab.33.000a31>
6. A.V. Kildishev, A. Boltasseva, V.M. Shalaev, Planar photonics with metasurfaces. *Science* **339**(6125), 1232009–1232009 (2013). <https://doi.org/10.1126/science.1232009>
7. A. Rubano, F. Cardano, B. Piccirillo, L. Marrucci, Q-plate technology: a progress review [Invited]. *J. Opt. Soc. of Am. B* **36**(5), D70–D87 (2019). <https://doi.org/10.1364/josab.36.000d70>
8. Y. Li, T. Zhan, Z. Yang, C. Xu, P.L. LiKamWa, K. Li, S.-T. Wu, Broadband cholesteric liquid crystal lens for chromatic aberration correction in catadioptric virtual reality optics. *Opt. Express* **29**(4), 6011–6020 (2021). <https://doi.org/10.1364/oe.419595>
9. A. Vijayakumar, B. Vinoth, I.V. Minin, J. Rosen, O.V. Minin, C.-J. Cheng, Experimental demonstration of square Fresnel zone plate with chiral side lobes. *Appl. Opt.* **56**(13), F128–F133 (2017). <https://doi.org/10.1364/ao.56.00f128>
10. F.-K. Bruder, T. Fäcke, R. Hagen, D. Hönel, T.P. Kleinschmidt, E. Orselli, C. Rewitz, T. Rölle, G. Walze, Diffractive optics in large sizes: computer-generated holograms (CGH) based on Bayfol HX photopolymer. *Adv. Display Technol.* (2015). <https://doi.org/10.1117/12.2077139>
11. J. Jahns, S. Sinzinger, Microoptics for biomedical applications. *Am. Biotechnol. Lab.* **11**, 53–54 (2000)
12. J. Jahns, A. Huang, Planar integration of free-space optical components. *Appl. Opt.* **28**(9), 1602–1605 (1989). <https://doi.org/10.1364/ao.28.001602>
13. H. Misawa, T. Kondo, S. Juodkazis, V. Mizeikis, S. Matsuo, Holographic lithography of periodic two- and three-dimensional microstructures in photoresist SU-8. *Opt. Express* **14**(17), 7943–7953 (2006). <https://doi.org/10.1364/oe.14.007943>
14. V. Anand, S.H. Ng, T. Katkus, S. Juodkazis, White light three-dimensional imaging using a quasi-random lens. *Opt. Express* **29**(10), 15551–15563 (2021). <https://doi.org/10.1364/oe.426021>
15. G. Seniutinas, G. Gervinskis, J. Anguita, D. Hakobyan, E. Braselet, S. Juodkazis, Nano-proximity direct ion beam writing. *Nanofabrication* **2**(1), 54–62 (2016). <https://doi.org/10.1515/nanofab-2015-0006>
16. A. Marcinkevičius, S. Juodkazis, M. Watanabe, M. Miwa, S. Matsuo, H. Misawa, J. Nishii, Femtosecond laser-assisted

- three-dimensional microfabrication in silica. *Opt. Lett.* **26**(5), 277–279 (2001). <https://doi.org/10.1364/ol.26.000277>
17. M. Malinauskas, A. Žukauskas, S. Hasegawa, Y. Hayasaki, V. Mizeikis, R. Buividas, S. Juodkakis, Ultrafast laser processing of materials: from science to industry. *Light Sci Appl* **5**(8), e16133 (2016). <https://doi.org/10.1038/lsa.2016.133>
 18. S. Juodkakis, K. Yamasaki, V. Mizeikis, S. Matsuo, H. Misawa, Formation of embedded patterns in glasses using femtosecond irradiation. *Appl. Phys. A* **79**, 1549–1553 (2004). <https://doi.org/10.1007/s00339-004-2845-1>
 19. E. Vanagas, I. Kudryashov, D. Tuzhilin, S. Juodkakis, S. Matsuo, H. Misawa, Surface nanostructuring of borosilicate glass by femtosecond nJ energy pulses. *Appl. Phys. Lett.* **82**(17), 2901–2903 (2003). <https://doi.org/10.1063/1.1570514>
 20. J. Rosen, A. Vijayakumar, M. Kumar, M.R. Rai, R. Kelner, Y. Kashter, A. Bulbul, S. Mukherjee, Recent advances in self-interference incoherent digital holography. *Adv. Opt. Photon.* **11**(1), 1–66 (2019). <https://doi.org/10.1364/aop.11.000001>
 21. Y. Kizuka, M. Yamaguchi, Y. Matsuoka, Characteristics of a laser beam spot focused by a binary diffractive axicon. *Opt. Eng.* **47**(5), 053401 (2008). <https://doi.org/10.1117/1.2919739>
 22. S.N. Khonina, A.P. Porfirev, 3D transformations of light fields in the focal region implemented by diffractive axicons. *Appl. Phys. B* **124**(9), 1–13 (2018). <https://doi.org/10.1007/s00340-018-7060-4>
 23. G. Gervinskas, G. Seniutinas, A. Vijayakumar, S. Bhattacharya, E. Jelmakas, A. Kadys, R. Tomašiūnas, S. Juodkakis, Fabrication and replication of micro-optical structures for growth of GaN-based light emitting diodes. *Micro Nano Mater. Dev. Syst.* (2013). <https://doi.org/10.1117/12.2033709>
 24. G. Andersen, D. Tullson, Broadband antihole photon sieve telescope. *Appl. Opt.* **46**(18), 3706–3708 (2007). <https://doi.org/10.1364/ao.46.003706>
 25. V. Anand et al., All femtosecond optical pump and X-ray probe: Holey-Axicon for free electron laser. *J. Phys. Photonics* **3**(2), 024002 (2021). <https://doi.org/10.1088/2515-7647/abd4ef>
 26. R. Menon, D. Gil, G. Barbastathis, H.I. Smith, Photon-sieve lithography. *J. Opt. Soc. Am. A* **22**(2), 342–345 (2005). <https://doi.org/10.1364/josaa.22.000342>
 27. R. Janeiro, R. Flores, P. Dahal, J. Viegas, Fabrication of a phase photon sieve on an optical fiber tip by focused ion beam nanomachining for improved fiber to silicon photonics waveguide light coupling. *Opt. Express* **24**(11), 11611–11625 (2016). <https://doi.org/10.1364/oe.24.011611>
 28. A. Vijayakumar, Y. Kashter, R. Kelner, J. Rosen, Coded aperture correlation holography—a new type of incoherent digital holograms. *Opt. Express* **24**(11), 12430–12441 (2016). <https://doi.org/10.1364/OE.24.012430>
 29. A. Vijayakumar, J. Rosen, Interferenceless coded aperture correlation holography—a new technique for recording incoherent digital holograms without two-wave interference. *Opt. Express* **25**(12), 13883–13896 (2017). <https://doi.org/10.1364/OE.25.013883>
 30. M.R. Rai, A. Vijayakumar, J. Rosen, Non-linear adaptive three-dimensional imaging with interferenceless coded aperture correlation holography (I-COACH). *Opt. Express* **26**(14), 18143–18154 (2018). <https://doi.org/10.1364/oe.26.018143>
 31. Y. Wan, C. Liu, T. Ma, Y. Qin, S. Lv, Incoherent coded aperture correlation holographic imaging with fast adaptive and noise-suppressed reconstruction. *Opt. Express* **29**(6), 8064–8075 (2021). <https://doi.org/10.1364/oe.418918>
 32. A. Vijayakumar, T. Katkus, S. Lundgaard, D.P. Linklater, E.P. Ivanova, S.H. Ng, S. Juodkakis, Fresnel incoherent correlation holography with single camera shot. *Opto Electron. Adv.* **3**(8), 200004 (2020). <https://doi.org/10.29026/oea.2020>
 33. R. Buividas, M. Mikutis, S. Juodkakis, Surface and bulk structuring of materials by ripples with long and short laser pulses: recent advances. *Prog. Quantum Electron* **38**(3), 119–156 (2014). <https://doi.org/10.1016/j.pquantelec.2014.03.002>
 34. E.G. Gamaly, A.V. Rode, Ultrafast re-structuring of the electronic landscape of transparent dielectrics: new material states (Die-Met). *Appl. Phys. A* **124**(3), 1–11 (2018). <https://doi.org/10.1007/s00339-018-1693-3>
 35. S. Juodkakis, Y. Nishi, H. Misawa, Femtosecond laser-assisted formation of channels in sapphire using KOH solution. *Phys. Status Solidi R* **2**(6), 275–277 (2008). <https://doi.org/10.1002/pssr.200802203>
 36. V. Anand, S.H. Ng, J. Maksimovic, D. Linklater, T. Katkus, E.P. Ivanova, S. Juodkakis, Single shot multispectral multidimensional imaging using chaotic waves. *Sci. Rep.* **10**(1), 13902 (2020). <https://doi.org/10.1038/s41598-020-70849-7>
 37. E. Vanagas, J. Kawai, D. Tuzilin, I. Kudryashov, A. Mizuyama, K.G. Nakamura, K. Kondo, S. Koshihara, M. Takesada, K. Matsuda, S. Juodkakis, V. Jarutis, S. Matsuo, H. Misawa, Glass cutting by femtosecond pulsed irradiation”. *J. Microlith. Microfab. Microsyst.* **3**(2), 358–363 (2004)
 38. J. Maksimovic, S.-H. Ng, T. Katkus, N.H. An Le, J.W.M. Chon, B.C.C. Cowie, T. Yang, Y. Bellouard, S. Juodkakis, Ablation in externally applied electric and magnetic fields. *Nanomaterials* **10**(2), 182 (2020). <https://doi.org/10.3390/nano10020182>
 39. J. Maksimovic, S.H. Ng, T. Katkus, B.C. Cowie, S. Juodkakis, External field-controlled ablation: magnetic field. *Nanomaterials* **9**(12), 1662 (2019). <https://doi.org/10.3390/nano9121662>
 40. J.-G. Hua, H. Ren, A. Jia, Z.-N. Tian, L. Wang, S. Juodkakis, Q.-D. Chen, H.-B. Sun, Convex silica microlens arrays via femtosecond laser writing. *Opt. Lett.* **45**(3), 636–639 (2020). <https://doi.org/10.1364/ol.378606>
 41. J.-G. Hua, Z.-N. Tian, S.-J. Xu, S. Lundgaard, S. Juodkakis, Fast fabrication of optical vortex generators by femtosecond laser ablation. *Appl. Surf. Sci.* **475**, 660–665 (2019). <https://doi.org/10.1016/j.apsusc.2018.12.249>
 42. K. Bundy, et al., FOBOS: a next-generation spectroscopic facility at the WM Keck observatory (2019). arXiv:1907.07195. Accessed 16 Jul 2019
 43. P. Caramazza, O. Moran, R. Murray-Smith, D. Faccio, Transmission of natural scene images through a multimode fibre. *Nat. Commun.* **10**, 2029 (2019). <https://doi.org/10.1038/s41467-019-10057-8>

Publisher's Note Springer Nature remains neutral with regard to jurisdictional claims in published maps and institutional affiliations.